Analyses of the Adhesion Interphase of Isotactic Polypropylene Using Hot-Melt Polyolefin Adhesives

Matsumoto, Takuya

Shimizu, Yosuke

Nishino, Takashi

(Citation)
Macromolecules,54(15):7226-7233

(Issue Date)
2021-08-10

(Resource Type)
journal article

(Version)
Accepted Manuscript

Analyses of Adhesion Interphase of *Isotactic* Polypropylene using Hot Melt Polyolefin Adhesives

Takuya Matsumoto[a], *Yousuke Shimizu*[a], *Takashi Nishino**[a]

[a] Department of Chemical Science and Engineering, Graduate School of Engineering, Kobe University, Rokko, Nada, Kobe, 657-8501, Japan

Key Word

Adhesion, interphase, *Isotactic* polypropylene, Hot melt polyolefin adhesive, Raman scattering, X-ray refraction contrast imaging, AFM

TOC

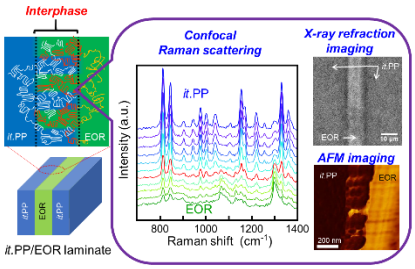
Interphase
it.PP
EOR
it.PP/EOR laminate
Confocal
Raman scattering
Intensity (a.u.)
it.PP
EOR
800
1000
1200
1400
Raman shift (cm-1)
X-ray refraction
imaging
it.PP
EOR
10 μm
AFM imaging
it.PP
EOR
200 nm

ABSTRACT

The interphase structure and properties of *isotactic* polypropylene (*it*.PP) have received much attention in the fundamental science and industrial applications for the improvement of the poor adhesion properties of the *it.*PP. In this work, we focused on the laminates with *it*.PP substrates and various ethylene-octene rubber (EOR) hot-melt adhesives with different molecular weight and crystallinity. We prepared laminate samples using EOR with low moleculaer weight (LWM-EOR), random copolymerized EOR (r-EOR), and block-like copolymerized EOR (b-EOR) as adhesives. We performed T-peel tests of the laminate samples and evaluated their thickness of the interphase with confocal Raman scattering imaging, X-ray refraction contrast imaging, and atomic force moicroscopic (AFM) imaging. The laminates with larger interphase thicknesses possessed the larger T-peel strengths, which was relatively consistent with these obtained results among all the measurement methods. It is revealed that the adhesion properties and the interphase thicknesses depended on the crystallinities of the *it.*PP substrates. These results mean that the interphase would be constructed by not only diffusion of molecular chains but also the crystalline growing and the formation of lamellae interlock in the interphase region.

Introduction

Boundary region between different materials is called as interface or interphase.[1–6] The former "interface" is used when the boundary can be considered as two-dimensional plane. On the contrary, the latter "interphase" regards the boundary as three- dimensional layer. In this paper, we employed "interphase" as described below. Interphase exists in narrow spatial and buried regions inside multicomponent materials and controls functional properties and mechanical performances of polymer materials. Therefore, the interphase plays a key role in the fields of composites,[4,7–11] polymer blends,[12–15] adhesion,[1,2,16,17] separators in electronic cells,[18,19] separation membranes[20,21] and laminates.[22,23] The investigation of structure and properties at the interphase is significant from the perspective of industrial developments as well as fundamental scientific insights. In particular, the structure and interaction at the interphase between components in polymer blends,[12–15] carbon fiber and polymer matrix in carbon-fiber-reinforced plastics,[5,24–28] and adhesives and metal or polymer substrates in adhered products[1,2,16,17,22,23] directly connects the reliability in material manufacturing. However, even in recent years, the discussion on interphase has been progressing based on probable prediction and it is a challenge that the region of the interphase was restricted spatially and buried into the bulk materials.

Recent drastic developments of the instruments for interfacial analyses and inspection have revealed not only the structure and properties of the interphase but also molecular behaviors of the polymer chains at the interphase. There are various candidates of instruments for the precise analyses of the interphase; for example, transmission electron microscope (TEM),[6,29–37] atomic force microscope (AFM),[38–41] confocal Raman scattering microspectroscope,[6,22,42–45] AFM-infrared spectroscope (AFM-IR),[46–49] sum frequency generation (SFG) vibrational spectroscope,[50–57] X-ray photoelectron spectroscope (XPS),[58–62] neutron reflectometry (NR),[63–66]

X-ray absorption fine structure (XAFS) measurement,[67,68] Rutherford scattering measurements,[69–71] and so on. These advanced analysis technologies provide the information at interphase including nanostructure, molecular orientation, distribution, and chemical bond states. The results from these various analyses of interphase were various, but sometimes their absolute values from the various analysis methods were different because of the diverse mechanism of analyses methods and various resolution. Therefore, the interphase analyses using multiple measurement methods with various mechanisms is significant.

The adhesive properties were decided by various factors including surface roughness of the adhered substrates, difference of surface free energies between substrates and adhesives, mechanical properties of adhesives and substrates, and adhesion interfacial structure. We also have previously reported on the correlation between adhesive strength and interfacial thickness of the *isotactic* polypropylene (*it*.PP)/cyanoacrylate ester instant adhesives using a confocal Raman scattering microspectroscope.[6] It is clarified that the primer treatment to *it*.PP substrates with cobalt complex primers provided larger adhesive strength as well as larger thickness of interfacial regions. In the industrial field, *it*.PP have been widely accepted as an attractive material because of its lightweight, proper mechanical properties and cost efficiency. In contrast, *it*.PP has a large disadvantage of its poor adhesion property, which is attributed to its non-polar chemical structure and crystallinity. To improve the poor adhesion properties, various surface modification and functionalized adhesives have been developed. Herein, we focused on the adhesion properties and interphase of the *it*.PP/hot-melt adhesive (HMA) laminates. We estimated the interphase thickness using not only confocal Raman scattering microspectroscopy but also X-ray refraction contrast measurement and AFM imaging observation, and then evaluated the effect of the crystallinity of the substrates and adhesives on interphase thickness and adhesive strength of the laminate samples.

2. Experiments

2.1. Materials

As adhesive substrates, *it*.PP (NOBLEN W501N, MFR at 230 °C = 8.5 g/10 min) was supplied from Sumitomo Chemical Co., Ltd.. Polyolefins as hot melt adhesives (HMAs) were low molecular weight ethylene-octene rubber (LMW-EOR) (Dow Chemical Japan Ltd., AFFINITY GA 1900, MFR at 190 ℃ = 1000 g/10 min), random copolymer ethylene-octene rubber (r-EOR) (Dow Chemical Japan Ltd., ENGAGE 8137, MFR at 190 ℃ = 13 g/10 min), block copolymer ethylene-octene rubber (b-EOR) (Dow Chemical Japan Ltd., INFUSE 9807, MFR at 190 ℃ = 15 g/10 min). These characteristic parameters were shown in Table 1. Xylene was purchased from Nakarai tesque Co., Ltd. and 1,2-dichlorobenzen-d_4 (≥98 atom%D) was purchased from Sigma-Aldrich. Co..

2.2. Characterization of *it*.PP substrate and EOR HMAs

Molecular structures of LMW-EOR, r-EOR and b-EOR were estimated by ^{1}H NMR (Bruker Co., Ltd., AVANCE III-400) at 400 MHz, 393 K. The NMR measurements were performed in 1,2-dichlorobenzen-d_4 solution. Wide angle X-ray diffraction profiles of LMW-EOR, r-EOR and b-EOR were measured with a X-ray diffractometer (Rigaku Co., Ltd., RINT 2000) at stepping interval 0.1°. The X-ray beam source was CuKα. The X-ray beam was operated at 40 kV and 20 mA. Differential scanning calorimetry (DSC) analysis was performed using a differential scanning calorimeter (Rigaku Co., Ltd., DSC8230) in nitrogen gas atmosphere. Heating and cooling rate was 5 ℃/min from room temperature to 200 ℃. Melting point and crystallization temperature

were evaluated from endothermic peak during heating process and exothermic peak during cooling process, respectively.

2.3. Preparation of *it*.PP/HMAs/*it*.PP laminates

As the adhered substrates, *it*.PP films were prepared by melt-pressing at 230 ℃ at 0 MPa, 6 MPa, and 0 MPa for 5 min respectively, followed by slowly cooling to room temperature. In the preparation of annealed *it*.PP substrates, after hot-pressing with the same condition, the samples were quenched into ice water and the *it*.PP films were annealed for 10 min. at 100 ℃, 130 ℃ and 150 ℃. All the thin HMA layers with the 20 μm thickness were obtained by solution-casting using 1%w/w xylene solution and drying at room temperature for 1 week. The HMA layer was sandwitched between two *it*.PP films and adhered to *it*.PP films by pressing at 150 ℃ at 1 MPa for 5 min, followed by cooling to room temperature.

2.4. T-peel test

T-peel strength of each laminate was evaluated using tensile tester (Shimadzu Co., Ltd., Autograph AGS-1kND) at 50 mm/min tensile rate, as shown in the Figure S8 in the Supporting Information. The substrates were trimmed with 60 mm ×15 mm of rectangles and the adhered area was 40 mm × 15 mm. The adhesive strength was obtained from the averages of the peeling strength of more than five species for every sample prepared under the same condition.

2.5. Raman scattering measurement

2.5.1. Preparation of cross section samples for Raman scattering measurement

Laminated films were embedded in epoxy resin (Bisphenol A/Epichlorhydrin : Triethylenetetramine = 15 : 2 (vol)), followed by curing at 40 ℃ for 12 h. Cross section of laminate films was fabricated by an ultra-microtome (Leica Microsystems GmbH., EM UC6), using a diamond knife (Syntek Co., Ltd., SYM Knife SYM2045). Cutting speed and cutting thickness were 10 mm/sec and 100 nm, respectively.

2.5.2. Single spot mode of Raman scattering measurement

Raman spectra of *it*.PP and HMA films were measured in the single spot mode by confocal nano-Raman spectroscope (WITec K. K., Alpha 300R). Nd/YAG semiconductor laser (wavelength: 532 nm) was used as an excitation laser. The laser intensity was 10 mW, the magnification of objective lens with numerical aperture 0.75 was ×50, the exposure time was 1 sec, the accumulation was 10 times, and the diffraction grating was 600 gr/mm.

2.5.3. Line scanning of Raman scattering measurement

Line scanning was employed to estimate interfacial thickness of laminates. Raman scattering spectra across the interphase of cross section of laminates were measured by step-by-step scanning with around 300 nm intervals, as shown in the Figure S9 in the Supporting Information. The spatial resolution in in-plane direction d_{xy} was defined by Hopkins's equation: $d_{xy} = k\lambda/NA$ (k: 0.51 at this apparatus, λ: wavelength, NA: numerical aperture). The value of d_{xy} was 362 nm. The laser intensity was 10 mW, the magnification of the objective lens was ×50 (Numerical aperture: 0.75), the exposure time was 1 sec, the accumulation was 10 times, and the diffraction grating was 600 gr/mm.

2.6. X-ray refraction contrast measurement

X-ray refraction contrast images of laminates were taken by high resolution X-ray microscope (Rigaku Co., Ltd., nano3DX) with rotating anode X-ray tube, as shown in Figure S10 in the Supporting Information. The X-ray source was CrKα and the X-ray beam was operated at 35 kV and 25 mA. The exposure time of X-ray beam was 10 sec, the magnification of objective lens was ×20, the spatial resolution was 0.27 μm^2/pixel, and the binning number was 1. The employed camera distances were 1 mm, 10 mm and 20 mm to estimate their interfacial thickness. The measured laminates were trimmed to 1 mm × 15 mm of recrtangles.

2.7. Atomic force microscopy

Topological and phase AFM images around the interfacial region between *it*.PP and HMAs were observed with an atomic force microscope (Hitachi High-tech Science Co., Ltd., NanoNavi/E-sweep) in the dynamic force mode. A silicon cantilever (Hitachi High-tech Science Co., Ltd., SI-DF20, spring constant: 15 N/m, tip radius: 10 nm) was employed as an AFM probe. The measured samples were prepared in the same method as those in the Raman scattering measurement.

2.8. Grazing incidence X-ray diffraction

Grazing incidence X-ray diffraction (GIXD) was performed with a high-resolution X-ray diffractometer (Rigaku Co., Ltd., SmartLab) in order to evaluate the surface crystallinity of *it*.PP films. The source of X-ray beam was CuKα. The X-ray beam was operated at 40 kV and 30 mA. Incident X-ray beam was irradiated with surface of *it*.PP film. For detecting diffracted X-ray, a scintillation counter was used. In the grazing incidence X-ray diffraction, X-ray penetration depth was determined by the wavelength of X-ray, the density of sample and X-ray incident angle α. The

critical angles is α_c, where the X-ray beam reflects totally at the substrate surface. GIXD to investigate on *it*.PP surface structure was performed at $\alpha = 0.1°$, which was smaller than α_c (0.147°). To evaluate crystallinity of *it.*PP films from the obtained X-ray diffraction profile, the method reported by Weidinger, Hermans, *et al* was employed.[72]

Results and Discussion

We evaluated the T-peel strength of *it*.PP/HMAs/*it*.PP laminates with LMW-EOR, r-EOR and b-EOR, which were commercially available and were accepted as hot-melt-adhesives for polyolefins. These EOR copolymers were composed of ethylene and octane units with the similar component fraction ratios from NMR charts in Figure S1-S3 in the Supporting Information and only the b-EOR adhesive possessed crystalline regions originated from ethylene units from X-ray diffraction profiles and DSC endotherm, as shown in Figure S4 and S7 in the Supporting Information. In contrast, only the amorphous regions were included in r-EOR as shown in Figure S4 and S6 in the Supporting Information. Therefore, these EOR adhesives were suitable for comparison of their adhesive strength and their interphase structure. The peeling strength was shown in Table 1 together with their characterization. The peeling strengths were increased in the order of LMW-EOR, r-EOR, and b-EOR. The fractural mode of laminates using LMW-EOR was cohesive fracture of adhesive itself and the interfacial peelings were observed in the laminates of r-EOR and b-EOR. The cohesive fracture of LMW-EOR was provided from the low mechanical strength of the LMW-EOR with lower molecular weight, while the laminates of the r-EOR and b-EOR adhesives were peeled at their interface between the EOR adhesives and *it*.PP substrates because the mechanical strength of the r-EPR and b-EOR were sufficiently strong.

Table 1. Melt flow rate (MFR), copolymer composition ratio, and density of EOR adhesives, and T-peel strength and fractural mode between *it*.PP and EOR laminates.

Adhesive sample	MFR	Ethylene	Octene	Density	T-peel strength	Fractural mode
	g/10min	mol%	mol%	g/cm^3	N/cm	
LMW-EOR	1,000	73	27	0.866	0.2±0.0	CF[a]
r-EOR	13	58	42	0.868	2.4±0.6	IF[b]

b-EOR	15	56	44	0.871	6.3±0.5	IF[b]

[a] Cohesive fracture of in the region of adhesive layers.
[b] Interfacial fracture.

For the evaluation of the interphase structure of *it.*PP/HMA laminates, we performed the observation of cross sections of the laminates using confocal Raman scattering scanning with the geometry across the interphase, as shown in Figure S9 in the Supporting Information. Before the investigation of the interphase, the Raman spectra of single components, *it.*PP, LMW-EOR, r-EOR, and b-EOR, were measured and shown in Figure S11 in the Supporting Information. In the Raman spectrum of *it.*PP, several well-defined band peaks were observed at 814 cm^{-1},1156 cm^{-1}, and 1332 cm^{-1}, while the bands in the spectra of all the EORs were detected at 1060 cm^{-1} and 1296 cm^{-1}.[73–77] The difference between the spectrum of *it.*PP substrates and those of each EOR adhesives was clearly observed. In the interfacial analysis, we also focused on the change of intensities of these bands at around interphase.

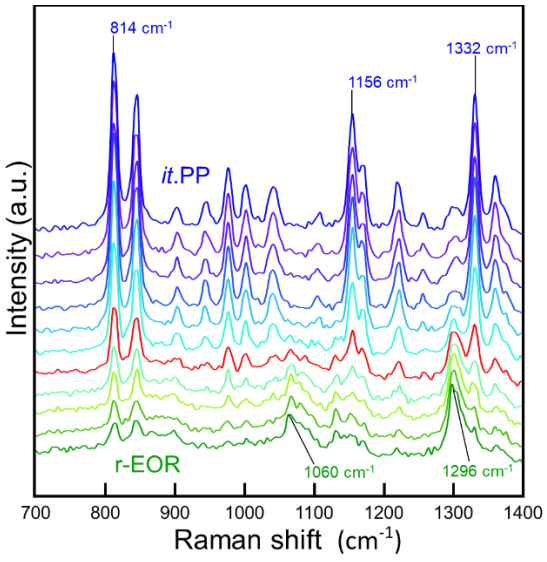

Figure 1. Raman scattering spectra across the interface between *it.*PP and r-EOR. Interval between the measurement positions of each spectrum was around 400 nm.

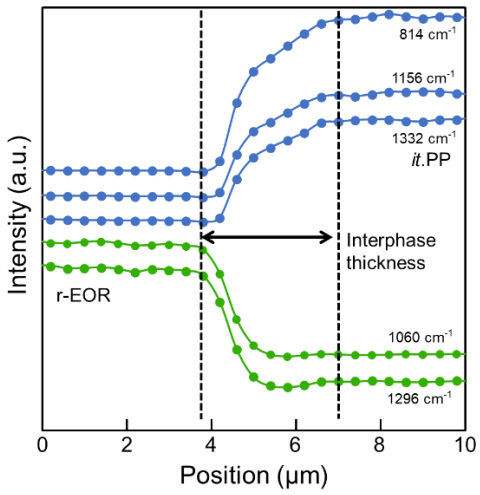

Figure 2. Intensity distribution plots of Raman bands across the interface of *it.*PP/r-EOR laminate.

Figure 1 shows the Raman spectra across interphase from the r-EOR adhesive side (bottom) to the *it*.PP substrate side (upper). In these Raman spectra, the bands originated from r-EOR gradually disappeared whereas those of *it.*PP emerged. At the interphase, the bands of the both components were observed, which means that both the components coexisted. The intensities of these bands were plotted at every measurement position across the interphase, as shown in Figure 2. As the measurement position was moved from r-EOR side to *it*.PP side, the intensities of the characteristic peak of r-EOR at 1060 cm^{-1} and 1296 cm^{-1}, which were originated from stretching of C−C bonds and twisting of CH_2 respectively, were decreased, whereas the intensities of the peaks of *it.*PP at 814 cm^{-1}, 1156 cm^{-1}, and 1332 cm^{-1}, which were originated from stretching of C−C bonds, stretching of C−C bonds and twisting and waging of CH_2 respectively, were increased in the interphase region.[73–77] We defined the region with the change of the components as “interphase thickness”, as shown in Figure 2. The interphase thickness of *it.*PP/r-EOR was 2.4 μm. The optical resolution of Raman scattering measurements was around 350 nm and the measurement steps of

the stages was 300 nm. Because the interphase thickness was much larger than these device resolution, the obtained value of the interphase thickness was significantly reasonable. The interphase thickness of *it.*PP/b-EOR/*it.*PP and *it.*PP/LMW-EOR/*it.*PP from Raman scattering measurements were also estimated and shown in Table 2. The thicknesses were increased in the order of LMW-EOR, r-EOR, and b-EOR. This order corresponded to those of their T-peel strengths. These results suggested the correlation between T-peel strengths and interphase thicknesses. We have previously reported on the dependence of T-peel strength on interphase thickness and primer treatment.[6] In this work, as the similar relation between T-peel strengths and interphase thicknesses without any primer treatment was observed, we suspected that the morphology and molecular behavior in the interphase region would have a large effect on their adhesive properties.

Table 2. Interphase thickness between *it*.PP and EORs laminates.

Adhesive sample	Interphase thickness		
	Raman	X-ray refraction	AFM
	μm	μm	nm
LMW-EOR	2.0±0.3	4.2±0.8	52±14
r-EOR	2.4±0.4	4.6±1.3	225±22
b-EOR	4.1±0.4	5.2±1.5	620±33

For the deeper investigation on the interphase thickness, other measurement methods with various instruments based on different analytical principle were performed; X-ray refraction contrast imaging and AFM observation with phase images. The widely accepted X-ray absorption contrast imaging is a method with the identification of the difference X-ray absorption coefficients of components in materials. Therefore, the optical resolution of instruments directly connects to the spatial resolution of the X-ray absorption contrast imaging methods. In contrast, in the X-ray

refraction contrast imaging, the refraction phenomena of X-ray at the interface between different components is employed, as shown in Figure S10 in the Supporting Information. In the X-ray refraction contrast measurements, the edges and interface of the observation subject are emphasized clearly and higher contrast resolution is achieved relative to the absorption contrast method.[78–80] Moreover, in the X-ray refraction contrast imaging, the edge region areas depend on the camera distance form a sample to a detector. Figure 3 shows an X-ray refraction contrast image and a gray value profile around interphase of a *it.*PP/r-EOR/*it.*PP laminate with 1 mm of camera distance. At the interphase between r-EOR and *it.*PP, the black region was observed and the thickness of black region was estimated as 4.7 μm. In addition, before the measurements, we evaluated the dependence on the thickness of sliced specimens and the tilts of samples to the X-ray beam. Figures S16 and S17 in the Supporting Information show the thickness of black region with various thickness of sliced specimens and tilt angles between samples and irradiated X-ray beam. As the thicknesses of sliced specimens had no effect on the thicknesses of black regions, the specimens with around 500 μm thickness were used. At a tilt angle, the minimum of the thickness of black region was observed. Therefore, in the X-ray refraction contrast measurements, the geometry, where the black region became narrowest, was controlled by rotating the sample after a sliced sample was mounted on the measurement stage. Moreover, we measured X-ray refraction contrast imaging of all the laminate samples with various camera distance using the geometries where the X-ray beam was irradiated form the direction parallel to the interphase of samples. To exclude the dependence of the camera distance L, the thickness of black region measured with various camera distance was plotted and the thickness at L = 0 was estimated by extrapolating to y-axis as shown in Figure 4. We defined the thickness at L = 0 as an interphase thickness in the X-ray refraction contrast measurement.

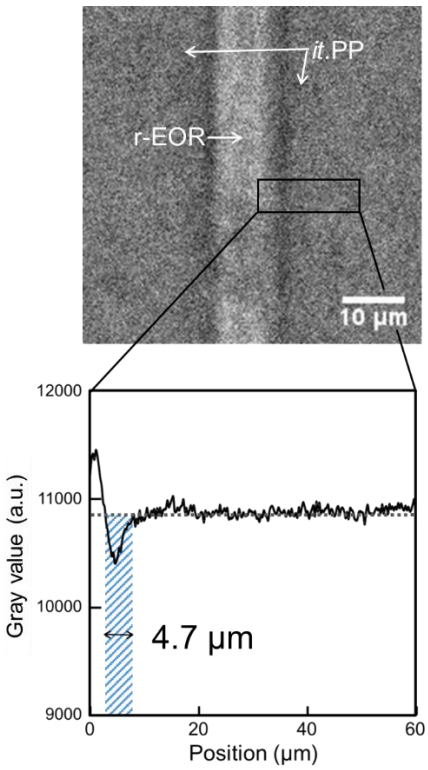

Figure 3. X-ray refraction contrast image and gray value profile of interface between *it.*PP and r-EOR. Camera distance L was 1 mm. The shadow region was defined as a black region.

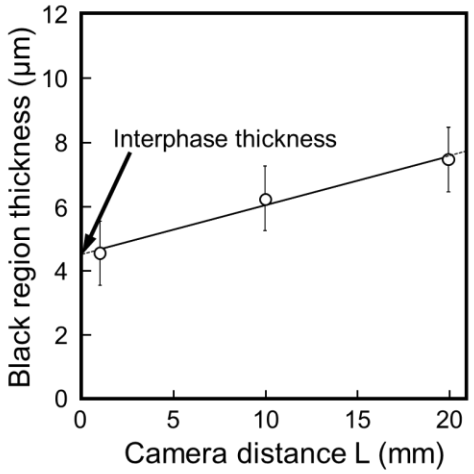

Figure 4. Plots of black region thicknesses and camera distance L of *it.*PP/r-EOR/*it.*PP laminates.

In Table 2, the estimated interphase thicknesses of laminates with LMW-EOR, r-EOR, and b-EOR in X-ray refraction contrast measurements are also shown. The thicknesses were increased in the order of the laminates of LMW-EOR, r-EOR, and b-EOR. The specimens with larger interphase thickness possessed larger T-peel strength. These relatively corresponded to the results of confocal Raman scattering imaging. The difference in the absolute values of the interphase thickness in Raman scattering imaging and X-ray refraction contrast measurement would be attributed the spatial resolution of these analysis methods. Actually, the spatial resolution of the X-ray contrast measurement was around 1 μm, which value was larger than 350 nm, that of Raman scattering imaging.

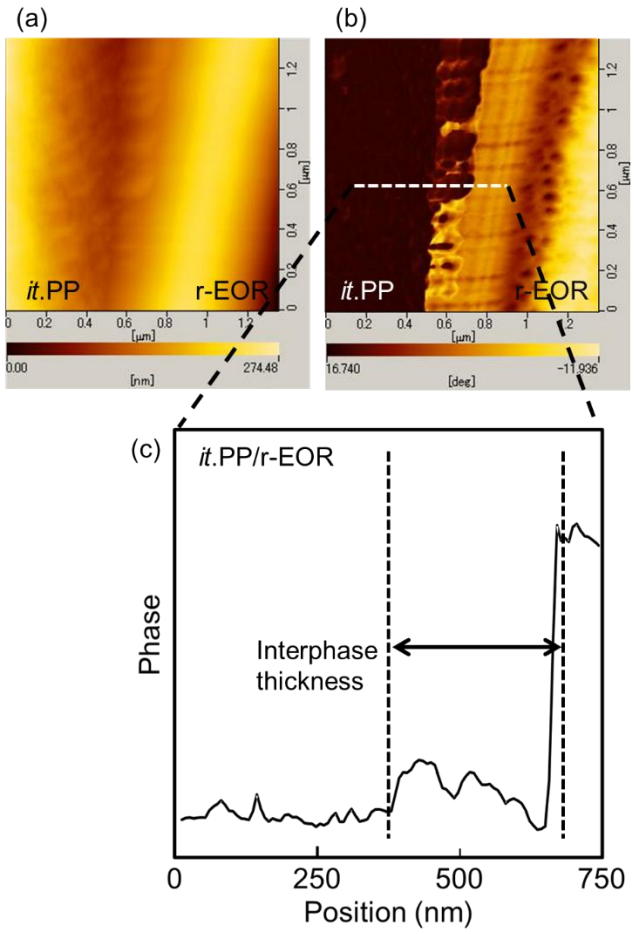

Figure 5. (a) Topological and (b) phase AFM images of *it.*PP/r-EOR/*it.*PP laminates and (c) profiles of phase contrast across interphase of *it.*PP/r-EOR/*it.*PP laminates.

In addition, we investigated on the interphase of the laminates with LMW-EOR, r-EOR, and b-EOR with AFM imaging. The topological and phase AFM images of the interphase of a *it.*PP/r-EOR/*it.*PP laminate sample are shown in Figure 5a and 5b, respectively. Around the interphase in the phase image, the *it.*PP substrate and the r-EOR adhesive were identified clearly. For all the other *it.*PP/EOR/*it.*PP laminates, the identification was observed in their phase images. These results mean that the difference in height around interphase was enough slight and the

identification in their phase images would be attributed to the difference of the components of these two layers. From the change of phase contrast around the interphase, the interphase region was defined, as shown in Figure 5c. The value of the interphase thickness was much lower than those estimated from Raman scattering imaging and X-ray refraction contrast imaging. These difference of the interphase thickness would be attributed to the spatial resolution and measurement mechanism of their analysis instruments. The resolutions of Raman spectroscopy, X-ray refraction contrast imaging and AFM imaging were 350 nm, 800 nm and <1.0 nm, respectively. Moreover, in the Raman spectroscopy, the chemical components was detected. In the X-ray refraction contrast imaging and AFM imaging, the difference of densities of the components and the mechanical properties of the components at the surface were measured, respectively. In contrast, the interphase thicknesses were increased in the order of LMW-EOR, r-EOR, and b-EOR, which was same trends as the results from the other measurements. These mean that the thicknesses observed in AFM images were also correlated to their T-peel strengths.

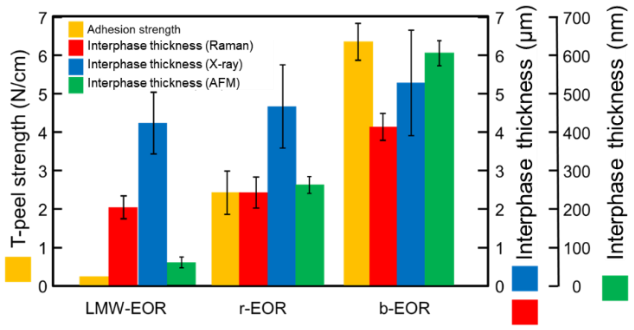

Figure 6. T-peel strengths and interphase thicknesses of *it*.PP/LMW-EOR/*it*.PP, *it*.PP/r-EOR/*it*.PP, and *it*.PP/b-EOR/*it*.PP laminates

Figure 6 summarized adhesive strengths and the interphase thicknesses obtained from all the measurements of all the *it*.PP/EOR/*it*.PP laminates. The laminates including EOR adhesives with

higher molecular weight and crystallinity possessed the larger peel strength and larger interphase thickness. In the laminating with hot-pressing, the mutual diffusion at the interface of amorphous polymer has been discussed. The molecular diffusion at the interface was controlled by the molecular weights. Polymer chains with low molecular weight are well-diffused and the crystallites restrict the dynamics of dynamics of polymer chains. For example, the diffusion distance of the polymer chains in polymer matrix can be estimated to be less than 100 nm from the Fick diffusion equation. However, the results in this study was inconsistent with the diffusion theory. Actually, the laminates of r-EOR and b-EOR with higher molecular weight possessed larger thicknesses of interphase as well as the laminate of crystalline b-EOR adhesive with high crystallinity showed the largest. The interphase thicknesses of r-EOR and b-EOR laminates were several micrometers from Raman scattering imaging and X-ray refraction contrast imaging, and even larger than 100 nm at least. These suggest that the formation of the interphase regions might not be solely depend on the diffusion of molecular chains around the interphase.

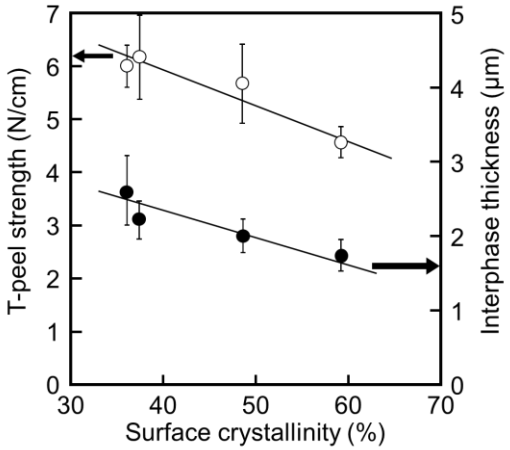

Figure 7. T-peel strength and interphase thickness of *it*.PP/b-EOR adhesives with various crystallinities of *it*.PP substrates.

For the investigation of the effect of crystallinity on the interphase thickness and adhesive strength, we measured the surface crystallinity, T-peel strength, and interphase thickness of the *it*.PP/EOR/*it*.PP laminates with various surface crystallinity of *it.*PP substrates. Their interphase thickness was evaluated by confoacal Raman scattering microscopy. The surface crystallinity of *it.*PP substrates was controlled by the annealing temperature from 100 °C to 150 °C. As shown in Figure 7, the *it*.PP/b-EOR/*it*.PP laminate with lower crystallinity showed higher adhesive strength and larger interphase thickness. On the contrary, the adhesive strength is independent of the substrate crystallinity for *it.*PP/r-EOR adhesives systems, where r-EOR showed no crystalline structures, as shown in Figure S28 in the Supporting Information. When laminating substrates with high crystallinity, the crystal growing of the substrates in the interphase region was reduced in the hot-press process. Therefore, the lower interphase thickness of *it.*PP substrates with higher crystallinity would be attributed to the decrease of crystal growing in hot-pressing process. It is suspected that the driving force of the formation of the interphase region might be provided from the interlock of lamellae such as “nanoanchor effect” and the interlock would reinforce the interphase region, as shown in Figure 8.

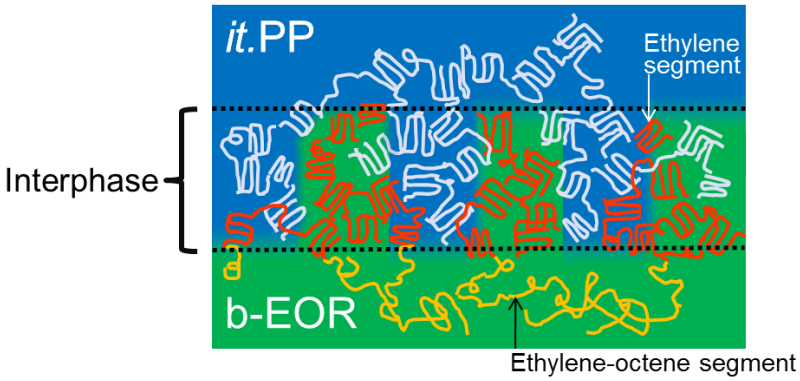

Figure 8. Illustration of the interphase of *it*.PP/b-EOR involving interlock of lamellae.

CONCLUSIONS

We performed the investigation on the interphase between *it.*PP substrates and ethylene-octene rubber (EOR) hot-melt adhesives, such as LMW-EOR, r-EOR, and b-EOR. For the evaluation of the interphase, we suggested and established the X-ray refraction contrast imaging methods. The results of the X-ray refraction contrast imaging methods well corresponded to those of confocal Raman scattering imaging and AFM imaging, which have been previously accepted for the investigation on the thickness. In addition, the larger interphase thickness provided the larger adhesion strength, from the comparison of the *it.*PP/LMW-EOR/*it.*PP, *it.*PP/r-EOR/*it.*PP, and *it.*PP/b-EOR/*it.*PP laminates. Moreover, the correlation of the interface crystallinity with the interphase thickness and adhesive strength was observed. Although only the diffusion of molecular chains has been discussed in the formation of the interface, it is revealed that the interphase region of the crystalline substrates and EOR adhesives was provided from the interlock of lamellae involving crystalline-growing, and the control of the crystalline growing in the interphase region was significant.

.

ASSOCIATED CONTENT

Supporting Information.

This material is including NMR charts, X-ray diffraction profiles, DSC curves, T-peel tests, Raman scanning method, X-ray refraction method, Raman spectra, intensity distribution of Raman bands across interphase, black band thickness in X-ray refraction methods, AFM images, phase contrast plots across interphase, crystallinities of the annealed substrates and relationships among crystallinities, T-peel strength and interphase thickness available free of charge via the Internet at http://

AUTHOR INFORMATION

Corresponding Author

*(T.N.) E-mail: tnishino@kobe-u.ac.jp

Funding Sources

This work was partially supported by JST-Mirai Program Grant Number JPMJMI18A2, Japan.

Notes

The authors declare no competing financial interest.

REFERENCES

(1) Sharpe, L. H. The Interphase in Adhesion. *J. Adhes.* **1972**, *4*, 51–64.

(2) Pukánszky, B. Interfaces and Interphases in Multicomponent Materials: Past, Present, Future. *Eur. Polym. J.* **2005**, *41*, 645–662.

(3) Park, S.-J.; Jin, J.-S. Effect of Silane Coupling Agent on Interphase and Performance of Glass Fibers/Unsaturated Polyester Composites. *J. Colloid Interface Sci.* **2001**, *242*, 174–179.

(4) Stöckelhuber, K. W.; Svistkov, A. S.; Pelevin, A. G.; Heinrich, G. Impact of Filler Surface Modification on Large Scale Mechanics of Styrene Butadiene/Silica Rubber Composites. *Macromolecules* **2011**, *44*, 4366–4381.

(5) Sharma, M.; Gao, S.; Mäder, E.; Sharma, H.; Wei, L. Y.; Bijwe, J. Carbon Fiber Surfaces and Composite Interphases. *Compos. Sci. Technol.* **2014**, *102*, 35–50.

(6) Matsumoto, T.; Nakanishi, Y.; Hongo, C.; Hakukawa, H.; Horiuchi, S.; Nishino, T. Adhesive Interphase Analyses of Isotactic Polypropylene and Cyanoacrylate with Cobalt Complex Primers. *Polymer* **2018**, *137*, 63–71.

(7) Liu, Y.; Kumar, S. Polymer/Carbon Nanotube Nano Composite Fibers–A Review. *ACS Appl. Mater. Interfaces* **2014**, *6*, 6069–6087.

(8) Ciprari, D.; Jacob, K.; Tannenbaum, R. Characterization of Polymer Nanocomposite Interphase and Its Impact on Mechanical Properties. *Macromolecules* **2006**, *39*, 6565–6573.

(9) Mortazavi, B.; Bardon, J.; Ahzi, S. Interphase Effect on the Elastic and Thermal Conductivity Response of Polymer Nanocomposite Materials: 3D Finite Element Study. *Comput. Mater. Sci.* **2013**, *69*, 100–106.

(10) Qiao, R.; Deng, H.; Putz, K. W.; Brinson, L. C. Effect of Particle Agglomeration and Interphase on the Glass Transition Temperature of Polymer Nanocomposites. *J. Polym. Sci. Part B Polym. Phys.* **2011**, *49*, 740–748.

(11) Brown, D.; Marcadon, V.; Mélé, P.; Albérola, N. D. Effect of Filler Particle Size on the Properties of Model Nanocomposites. *Macromolecules* **2008**, *41*, 1499–1511.

(12) Elias, L.; Fenouillot, F.; Majeste, J. C.; Cassagnau, P. Morphology and Rheology of Immiscible Polymer Blends Filled with Silica Nanoparticles. *Polymer* **2007**, *4*, 6029–6040.

(13) Mijovic, J.; Sy, J.-W.; Kwei, T. K. Reorientational Dynamics of Dipoles in Poly(Vinylidene Fluoride)/Poly(Methyl Methacrylate) (PVDF/PMMA) Blends by Dielectric Spectroscopy. *Macromolecules* **1997**, *30*, 3042–3050.

(14) Ajji, A.; Utracki, L. A. Interphase and Compatibilization of Polymer Blends. *Polym. Eng. Sci.* **1996**, *36*, 1574–1585.

(15) Utracki, L. A. Compatibilization of Polymer Blends. *Can. J. Chem. Eng.* **2002**, *80*, 1008–1016.

(16) Boesel, L. F.; Greiner, C.; Arzt, E.; del Campo, A. Gecko-Inspired Surfaces: A Path to Strong and Reversible Dry Adhesives. *Adv. Mater.* **2010**, *22*, 2125–2137.

(17) Liston, E. M.; Martinu, L.; Wertheimer, M. R. Plasma Surface Modification of Polymers for Improved Adhesion: A Critical Review. *J. Adhes. Sci. Technol.* **1993**, *7*, 1091–1127.

(18) Zhang, X.; Wang, S.; Xue, C.; Xin, C.; Lin, Y.; Shen, Y.; Li, L.; Nan, C.-W. Self-Suppression of Lithium Dendrite in All-Solid-State Lithium Metal Batteries with Poly(Vinylidene Difluoride)-Based Solid Electrolytes. *Adv. Mater.* **2019**, *31*, 1806082.

(19) Li, F.-S.; Wu, Y.-S.; Chou, J.; Winter, M.; Wu, N.-L. A Mechanically Robust and Highly Ion-Conductive Polymer-Blend Coating for High-Power and Long-Life Lithium-Ion Battery Anodes. *Adv. Mater.* **2015**, *27*, 130–137.

(20) Sackmann, E. Supported Membranes: Scientific and Practical Applications. *Science* **1996**, *271*, 43–48.

(21) Pincus, P. Colloid Stabilization with Grafted Polyelectrolytes. *Macromolecules* **1991**, *24*, 2912–2919.

(22) Kotera, M.; Urushihara, Y.; Izumo, D.; Nishino, T. Interfacial Structure of All-Polyethylene Laminate Using Scanning Thermal Microscope and Nano-Raman Spectroscope. *Polymer* **2012**, *53*, 1966–1971.

(23) Kotera, M.; Nishino, T.; Taura, T.; Saito, M.; Nakai, A.; Koyama, T.; Kagoshima, Y. Interfacial Structure Analysis of Polymer Laminate Using SPring-8 X-Ray Microbeam. *Compos. Interfaces* **2007**, *14*, 63–72.

(24) Qin, W.; Vautard, F.; Drzal, L. T.; Yu, J. Mechanical and Electrical Properties of Carbon Fiber Composites with Incorporation of Graphene Nanoplatelets at the Fiber–Matrix Interphase. *Compos. Part B Eng.* **2015**, *69*, 335–341.

(25) Thostenson, E. T.; Li, W. Z.; Wang, D. Z.; Ren, Z. F.; Chou, T. W. Carbon Nanotube/Carbon Fiber Hybrid Multiscale Composites. *J. Appl. Phys.* **2002**, *91*, 6034–6037.

(26) Ning, F.; Cong, W.; Qiu, J.; Wei, J.; Wang, S. Additive Manufacturing of Carbon Fiber Reinforced Thermoplastic Composites Using Fused Deposition Modeling. *Compos. Part B Eng.* **2015**, *80*, 369–378.

(27) Schultz, J.; Lavielle, L.; Martin, C. The Role of the Interface in Carbon Fibre-Epoxy Composites. *J. Adhes.* **1987**, *23*, 45–60.

(28) Drzal, L. T.; Madhukar, M. Fibre-Matrix Adhesion and Its Relationship to Composite Mechanical Properties. *J. Mater. Sci.* **1993**, *28*, 569–610.

(29) Horiuchi, S.; Terasaki, N.; Itabashi, M. Evaluation of the Properties of Plastic-Metal Interfaces Directly Bonded via Injection Molding. *Manuf. Rev.* **2020**, *7*, 11.

(30) Lyu, L.; Ohnuma, Y.; Shigemoto, Y.; Hanada, T.; Fukada, T.; Akiyama, H.; Terasaki, N.; Horiuchi, S. Toughness and Durability of Interfaces in Dissimilar Adhesive Joints of Aluminum and Carbon-Fiber-Reinforced Thermoplastics. *Langmuir* **2020**, *36*, 14046–14057.

(31) Yin, Z.; Koulic, C.; Pagnoulle, C.; Jérôme, R. Probing of the Reaction Progress at a PMMA/PS Interface by Using Anthracene-Labeled Reactive PS Chains. *Langmuir* **2003**, *19*, 453–457.

(32) Laoutid, F.; Estrada, E.; Michell, R. M.; Bonnaud, L.; Müller, A. J.; Dubois, P. The Influence of Nanosilica on the Nucleation, Crystallization and Tensile Properties of PP–PC and PP–PA Blends. *Polymer* **2013**, *54*, 3982–3993.

(33) Jiao, J.; Kramer, E. J.; de Vos, S.; Möller, M.; Koning, C. Morphological Changes of a Molten Polymer/Polymer Interface Driven by Grafting. *Macromolecules* **1999**, *32*, 6261–6269.

(34) Lancin, M.; Marhic, C. TEM Study of Carbon Fibre Reinforced Aluminium Matrix Composites: Influence of Brittle Phases and Interface on Mechanical Properties. *J. Eur. Ceram. Soc.* **2000**, *20*, 1493–1503.

(35) Zhai, L. L.; Ling, G. P.; Wang, Y. W. Effect of Nano-Al_2O_3 on Adhesion Strength of Epoxy Adhesive and Steel. *Int. J. Adhes. Adhes.* **2008**, *28*, 23–28.

(36) Yoshida, Y.; Yoshihara, K.; Nagaoka, N.; Hayakawa, S.; Torii, Y.; Ogawa, T.; Osaka, A.; Meerbeek, B. V. Self-Assembled Nano-Layering at the Adhesive Interface. *J. Dent. Res.* **2012**, *91*, 376–381.

(37) Liu, Y.; Shigemoto, Y.; Hanada, T.; Miyamae, T.; Kawasaki, K.; Horiuchi, S. Role of Chemical Functionality in the Adhesion of Aluminum and Isotactic Polypropylene. *ACS Appl. Mater. Interfaces* **2021**, *13*, 11497–11506.

(38) Tsui, O. K. C.; Wang, X. P.; Ho, J. Y. L.; Ng, T. K.; Xiao, X. Studying Surface Glass-to-Rubber Transition Using Atomic Force Microscopic Adhesion Measurements. *Macromolecules* **2000**, *33*, 4198–4204.

(39) Carpick, R. W.; Agraït, N.; Ogletree, D. F.; Salmeron, M. Variation of the Interfacial Shear Strength and Adhesion of a Nanometer-Sized Contact. *Langmuir* **1996**, *12*, 3334–3340.

(40) Lafranche, E.; Macedo, S.; Ferreira, P.; Martins, C. I. Thin Wall Injection-Overmoulding of Polyamide 6/Polypropylene Multilayer Parts: PA6/PP-g-Ma Interfacial Adhesion Investigations. *J. Appl. Polym. Sci.* **2021**, *138*, 50294.

(41) Gao, S.-L.; Mäder, E. Characterisation of Interphase Nanoscale Property Variations in Glass Fibre Reinforced Polypropylene and Epoxy Resin Composites. *Compos. Part A Appl. Sci. Manuf.* **2002**, *33*, 559–576.

(42) Hajatdoost, S.; Olsthoorn, M.; Yarwood, J. Depth Profiling Study of Effect of Annealing Temperature on Polymer/Polymer Interfaces in Laminates Using Confocal Raman Microspectroscopy. *Appl. Spectrosc.* **1997**, *51*, 1784–1790.

(43) Casdorff, K.; Kläusler, O.; Gabriel, J.; Amen, C.; Lehringer, C.; Burgert, I.; Keplinger, T. About the Influence of a Water-Based Priming System on the Interactions between Wood

and One-Component Polyurethane Adhesive Studied by Atomic Force Microscopy and Confocal Raman Spectroscopy Imaging. *Int. J. Adhes. Adhes.* **2018**, *80*, 52–59.

(44) Abiko, K.; Kato, Y.; Hohjo, H.; Kishida, Y.; Sudo, E. Raman Imaging of Residual Stress Distribution in Epoxy Resin and Metal Interface. *J. Raman Spectrosc.* **2020**, *51*, 193–200.

(45) Fukuri, N.; Ougizawa, T. Confocal Raman Spectroscopy Studies on the Mutual Diffusion Behavior at the Interface between Two Different Polyesters. *Polym. Eng. Sci.* **2018**, *58*, 991–997.

(46) Cavezza, F.; Pletincx, S.; Revilla, R. I.; Weaytens, J.; Boehm, M.; Terryn, H.; Hauffman, T. Probing the Metal Oxide/Polymer Molecular Hybrid Interfaces with Nanoscale Resolution Using AFM-IR. *J. Phys. Chem. C* **2019**, *123*, 26178–26184.

(47) Zhao, S.; Kimura, F.; Wang, S.; Kajihara, Y. Chemical Interaction at the Interface of Metal–Plastic Direct Joints Fabricated via Injection Molded Direct Joining. *Appl. Surf. Sci.* **2021**, *540*, 148339.

(48) Morsch, S.; Liu, Y.; Malanin, M.; Formanek, P.; Eichhorn, K.-J. Exploring Whether a Buried Nanoscale Interphase Exists within Epoxy–Amine Coatings: Implications for Adhesion, Fracture Toughness, and Corrosion Resistance. *ACS Appl. Nano Mater.* **2019**, *2*, 2494–2502.

(49) Sang, J.; Sato, R.; Aisawa, S.; Hirahara, H.; Mori, K. Hybrid Joining of Polyamide and Hydrogenated Acrylonitrile Butadiene Rubber through Heat-Resistant Functional Layer of Silane Coupling Agent. *Appl. Surf. Sci.* **2017**, *412*, 121–130.

(50) Aoki, M.; Shundo, A.; Okamoto, K.; Ganbe, T.; Tanaka, K. Segregation of an Amine Component in a Model Epoxy Resin at a Copper Interface. *Polym. J.* **2019**, *51*, 359–363.

(51) Lu, X.; Shephard, N.; Han, J.; Xue, G.; Chen, Z. Probing Molecular Structures of Polymer/Metal Interfaces by Sum Frequency Generation Vibrational Spectroscopy. *Macromolecules* **2008**, *41*, 8770–8777.

(52) Li, B.; Andre, J. S.; Chen, X.; Walther, B.; Paradkar, R.; Feng, C.; Tucker, C.; Mohler, C.; Chen, Z. Probing Molecular Behavior of Carbonyl Groups at Buried Nylon/Polyolefin Interfaces in Situ. *Langmuir* **2020**, *36*, 11349–11357.

(53) Li, B.; Andre, J. S.; Chen, X.; Walther, B.; Paradkar, R.; Feng, C.; Tucker, C.; Mohler, C.; Chen, Z. Observing a Chemical Reaction at a Buried Solid/Solid Interface in Situ. *Anal. Chem.* **2020**, *92*, 14145–14152.

(54) Zhang, S.; Andre, J. S.; Hsu, L.; Toolis, A.; Esarey, S. L.; Li, B.; Chen, Z. Nondestructive In Situ Detection of Chemical Reactions at the Buried Interface between Polyurethane and Isocyanate-Based Primer. *Macromolecules* **2020**, *53*, 10189–10197.

(55) Andre, J. S.; Li, B.; Chen, X.; Paradkar, R.; Walther, B.; Feng, C.; Tucker, C.; Mohler, C.; Chen, Z. Interfacial Reaction of a Maleic Anhydride Grafted Polyolefin with Ethylene Vinyl Alcohol Copolymer at the Buried Solid/Solid Interface. *Polymer* **2021**, *212*, 123141.

(56) Miyamae, T.; Taga, Y. Characterisation of Buried Glass/Cyclo-Olefin Polymer Film Interfaces by Sum-Frequency Generation Vibrational Spectroscopy. *J. Adhes.* **2018**, *94*, 1155–1167.

(57) Sensui, K.; Tarui, T.; Miyamae, T.; Sato, C. Evidence of Chemical-Bond Formation at the Interface between an Epoxy Polymer and an Isocyanate Primer. *Chem. Commun.* **2019**, *55*, 14833–14836.

(58) Tao, G.; Gong, A.; Lu, J.; Sue, H.-J.; Bergbreiter, D. E. Surface Functionalized Polypropylene: Synthesis, Characterization, and Adhesion Properties. *Macromolecules* **2001**, *34*, 7672–7679.

(59) Bou, M.; Martin, J. M.; Le Mogne, T.; Vovelle, L. Chemistry of the Interface between Aluminium and Polyethyleneterephthalate by XPS. *Appl. Surf. Sci.* **1991**, *47*, 149–161.

(60) Boucher, E.; Folkers, J. P.; Hervet, H.; Léger, L.; Creton, C. Effects of the Formation of Copolymer on the Interfacial Adhesion between Semicrystalline Polymers. *Macromolecules* **1996**, *29*, 774–782.

(61) Inagaki, N.; Tasaka, S.; Masumoto, M. Improved Adhesion between Kapton Film and Copper Metal by Plasma Graft Polymerization of Vinylimidazole. *Macromolecules* **1996**, *29*, 1642–1648.

(62) Lee, W.-J.; Lee, Y.-S.; Rha, S.-K.; Lee, Y.-J.; Lim, K.-Y.; Chung, Y.-D.; Whang, C.-N. Adhesion and Interface Chemical Reactions of Cu/Polyimide and Cu/TiN by XPS. *Appl. Surf. Sci.* **2003**, *205*, 128–136.

(63) Stoffel, N. C.; Dai, C.-A.; Kramer, E. J.; Russell, T. P.; Deline, V.; Volksen, W.; Wu, W.; Satija, S. High-Resolution Profiling of the Polyimide−Polyimide Interface. *Macromolecules* **1996**, *29*, 6880–6891.

(64) Chennevière, A.; Drockenmuller, E.; Damiron, D.; Cousin, F.; Boué, F.; Restagno, F.; Léger, L. Quantitative Analysis of Interdigitation Kinetics between a Polymer Melt and a Polymer Brush. *Macromolecules* **2013**, *46*, 6955–6962.

(65) Hayashi, T.; Segawa, K.; Sadakane, K.; Fukao, K.; Yamada, N. L. Interfacial Interaction and Glassy Dynamics in Stacked Thin Films of Poly(Methyl Methacrylate). *J. Chem. Phys.* **2017**, *146*, 203305.

(66) Kawaguchi, D.; Nelson, A.; Masubuchi, Y.; Majewski, J. P.; Torikai, N.; Yamada, N. L.; Siti Sarah, A. R.; Takano, A.; Matsushita, Y. Precise Analyses of Short-Time Relaxation at Asymmetric Polystyrene Interface in Terms of Molecular Weight by Time-Resolved Neutron Reflectivity Measurements. *Macromolecules* **2011**, *44*, 9424–9433.

(67) Oura, M.; Ishihara, T.; Osawa, H.; Yamane, H.; Hatsui, T.; Ishikawa, T. Development of a Scanning Soft X-Ray Spectromicroscope to Investigate Local Electronic Structures on Surfaces and Interfaces of Advanced Materials under Conditions Ranging from Low Vacuum to Helium Atmosphere. *J. Synchrotron Radiat.* **2020**, *27*, 664–674.

(68) Yamane, H.; Oura, M.; Takahashi, O.; Fons, P.; Varadwaj, P. R.; Shimoi, Y.; Ohkubo, M.; Ishikawa, T.; Yamazaki, N.; Hasegawa, K.; Takgi, K.; Hatsui, T. Soft X-Ray Absorption Spectroscopy Probes OH···π Interactions in Epoxy-Based Polymers. *J. Phys. Chem. C* **2020**, *124*, 9622–9627.

(69) Jablonski, E. L.; Gorga, R. E.; Narasimhan, B. Interdiffusion and Phase Behavior at Homopolymer/Random Copolymer Interfaces. *Polymer* **2003**, *44*, 729–741.

(70) Thompson, R. L.; Gurumurthy, S. C.; Pattabi, M. Depth Distribution of Silver Particulate Films Deposited in Softened Polystyrene Substrates Studied through Rutherford Backscattering Spectrometry. *J. Appl. Phys.* **2011**, *110*, 43533.

(71) Gurumurthy, C.; Kramer, E. J.; Hui, C.-Y. Controlling Interfacial Interpenetration and Fracture Properties of Polyimide/Epoxy Interfaces. *J. Adhes.* **2006**, *82*, 239–266.

(72) Weidinger, A.; Hermans, P. H. On the Determination of the Crystalline Fraction of Isotactic Polypropylene from X-Ray Diffraction. *Die Makromol. Chemie* **1961**, *50*, 98–115.

(73) Lieser, G.; Wegner, G.; Smith, J. A.; Wagener, K. B. Morphology and Packing Behavior of Model Ethylene/Propylene Copolymers with Precise Methyl Branch Placement. *Colloid Polym. Sci.* **2004**, *282*, 773–781.

(74) Furukawa, T.; Watari, M.; Siesler, H. W.; Ozaki, Y. Discrimination of Various Poly(Propylene) Copolymers and Prediction of Their Ethylene Content by near-Infrared and Raman Spectroscopy in Combination with Chemometric Methods. *J. Appl. Polym. Sci.* **2003**, *87*, 616–625.

(75) Simanke, A. G.; Galland, G. B.; Freitas, L.; da Jornada, J. A. H.; Quijada, R.; Mauler, R. S. Influence of the Comonomer Content on the Thermal and Dynamic Mechanical Properties of Metallocene Ethylene/1-Octene Copolymers. *Polymer* **1999**, *40*, 5489–5495.

(76) Tadokoro, H.; Kobayashi, M.; Ukita, M.; Yasufuku, K.; Murahashi, S.; Torii, T. Normal Vibrations of the Polymer Molecules of Helical Conformation. V. Isotactic Polypropylene and Its Deuteroderivatives. *J. Chem. Phys.* **1965**, *42*, 1432–1449.

(77) Ran, S.; Fang, D.; Sics, I.; Toki, S.; Hsiao, B. S.; Chu, B. Combined Techniques of Raman Spectroscopy and Synchrotron Two-Dimensional X-Ray Diffraction for in Situ Study of Anisotropic System: Example of Polymer Fibers under Deformation. *Rev. Sci. Instrum.* **2003**, *74*, 3087–3092.

(78) Wilkins, S. W.; Gureyev, T. E.; Gao, D.; Pogany, A.; Stevenson, A. W. Phase-Contrast Imaging Using Polychromatic Hard X-Rays. *Nature* **1996**, *384*, 335–338.

(79) Wen, H.; Gomella, A. A.; Patel, A.; Lynch, S. K.; Morgan, N. Y.; Anderson, S. A.; Bennett, E. E.; Xiao, X.; Liu, C.; Wolfe, D. E. Subnanoradian X-Ray Phase-Contrast Imaging Using a Far-Field Interferometer of Nanometric Phase Gratings. *Nat. Commun.* **2013**, *4*, 2659.

(80) Sunaguchi, N.; Yuasa, T.; Huo, Q.; Ichihara, S.; Ando, M. X-Ray Refraction-Contrast Computed Tomography Images Using Dark-Field Imaging Optics. *Appl. Phys. Lett.* **2010**, *97*, 153701.